A&A, 700, L6 (2025)
https://doi.org/10.1051/0004-6361/202555902

Astronomy & Astrophysics

LETTER TO THE EDITOR

Detection of SiC_6 in IRC +10216 through *Q*-band lines

J. R. Pardo[1,2,⋆], J. P. Fonfría[1], M. Agúndez[1], B. Tercero[3,4], C. Cabezas[1], L. Velilla-Prieto[1], M. Guélin[5], P. de Vicente[3,4], and J. Cernicharo[1,⋆]

[1] Consejo Superior de Investigaciones Científicas, Instituto de Física Fundamental, C/ Serrano 121, 28006 Madrid, Spain
[2] Centre National de la Recherche Scientifique, Observatoire de Paris, 77 Avenue Denfert Rochereau, 75014 Paris, France
[3] Centro de Desarrollos Tecnológicos, Observatorio de Yebes (IGN), 19141 Yebes, Guadalajara, Spain
[4] Observatorio Astronómico Nacional (OAN, IGN), Madrid, Spain
[5] Institut de Radioastronomie Millimétrique, 300 rue de la Piscine, F-38406 Saint Martin d'Hères, France

Received 11 June 2025 / Accepted 14 July 2025

ABSTRACT

Ongoing *Q*-band (31–50 GHz) integrations on IRC +10216 with the Yebes 40m telescope have now reached the level of sub-mK noise, with hundreds of new lines arising above the 3σ detection limit. Among them is a new, harmonically related series with integer quantum numbers ranging from J_{up} = 26 to 40, which has allowed it to be assigned to SiC_6. We clearly detected a total of nine isolated (or otherwise not critically blended) spectral features, with peak intensities around or slightly below 1 mK in the T_A^* scale, thanks to the extremely low noise in the spectra. Five additional lines were seen to be partially blended with lines from other species, but could still be relatively well modeled due to the uniformity of the characteristic U-shaped line profiles emerge from the envelope of IRC+10216. As a result, we built a rotation diagram for SiC_6, providing a column density of $\sim 8 \times 10^{11}$ cm^{-2} and a rotational temperature around 19 K. A similar analysis was done for SiC_4, $^{29}SiC_4$, and $^{30}SiC_4$. Together, these insights offer the first view at the chemistry of linear silicon carbides in IRC+10216.

Key words. astrochemistry – line: identification – molecular data – stars: carbon – stars: individual: IRC +10216

1. Introduction

The search for new molecules in astronomical sources requires extremely deep integrations as the list of already known species continues growing. For this task, it is important to count on constantly updated line catalogs that help us to spot unidentified features among an increasing forest of lines from identified species. These new findings, however, are important not just for extending the list but for the many questions opened up by their presence in the astronomical sources, such as formation paths, physical conditions, and growth of chemical complexity. Long molecules, large polycyclic aromatic hydrocarbons (PAHs), cations and anions, rare isomers, and high vibrational states, are all being found as the sensitivity of the surveys reaches sub-mK levels in TMC-1 and IRC+10216 within the ERC synergy project Nanocosmos[1].

Many new species have been found directly in TMC-1 and IRC+10216 without any previous laboratory information on their frequencies. This is due to the difficulty to obtain their spectra in the laboratory. It is the case for cations, radicals, and metal-bearing species involving Mg, Ca, Al, and Na (Cernicharo et al. 2019; Pardo et al. 2021; Cabezas et al. 2023; Cernicharo et al. 2023a). Nevertheless, in some cases, the main driver for molecular discoveries of metal-bearing species has been new laboratory work (Changala et al. 2022; Gupta et al. 2024). For IRC+10216, additional *Q*-band observations have been added until September 15, 2024, improving the sensitivity by a factor of more than 2. This widens the opportunities for identifying new molecular species and new isotopic substitutions, isomers, and vibrationally excited states of already known species, helping to complete the chemical picture of this source (see, e.g., Cernicharo et al. 2023b,a; Cabezas et al. 2023).

In this Letter, we report the detection of SiC_6 through 14 rotational lines, of which 9 are unblended or weakly blended at the observed sub-mK peak intensities, but well above the 3σ limit. Rotation diagrams, from which a column density and a rotational temperature can be determined, are established for SiC_6, and for SiC_4, $^{29}SiC_4$, and $^{30}SiC_4$ that also appear in our data. All this information has been analyzed as in our previous studies (Pardo et al. 2022; Cernicharo et al. 2023b,a; Cabezas et al. 2023).

Section 2 gives an update on the status of this large observational program and describes the way we accumulated the data through such a long period of time. Section 3 is aimed at describing the procedure for fitting the data using a double-horned line-shaped function, typical of expanding envelopes. This section also deals with the fact that lines can sometimes be heavily blended. The spectra of SiC_6, SiC_4, $^{29}SiC_4$, and $^{30}SiC_4$ are presented in Section 4 and their derived physical parameters are discussed in Section 5 on the ground of chemical models, followed by the final conclusions of this work.

2. Observations and data accumulation

The data presented in this Letter come from an ongoing 31–50 GHz spectral survey of IRC+10216 carried out with the 40 meter antenna of the Yebes Observatory (IGN, Spain; hereafter Yebes-40m), after several improvements in its equipment

⋆ Corresponding authors: jr.pardo@csic.es, jose.cernicharo@csic.es
[1] https://nanocosmos.iff.csic.es/

funded by Nanocosmos. The data was obtained after accumulation of 1360 hours of on-source telescope time in 480 observing sessions from April 14, 2019 to September 15, 2024. The experimental setup has been described in detail by Tercero et al. (2021). The antenna provides a main beam efficiency from 0.6 at 31 GHz to 0.43 at 50 GHz and a beam size in the range 36–56″ for those frequencies (45″at 39.2 GHz). The Nanocosmos Q-band receiver uses two HEMT cold amplifiers covering the 31.0–50.3 GHz frequency range with horizontal and vertical polarizations. The backends are 16 × 2.5 GHz fast Fourier transform spectrometers (FFTS), with a primary spectral resolution of 38.1 kHz. The observing mode was position switching with an off position at 300″ away in azimuth from the reference $\alpha_{J2000} = 09^h\ 47^m\ 57.36^s$ and $\delta_{J2000} = +13°\ 16'44.4''$ position used for IRC+10216. Pointing corrections were obtained by observing the SiO masers of R Leo, and errors were always within 2–3″. The intensity scale of the final calibrated data is antenna temperature (T_A^*) corrected for atmospheric absorption using the ATM package (Cernicharo 1985; Pardo et al. 2001, 2025). The calibration uncertainties are estimated to be within 10%.

The receiver temperature improvements during this long project, along with the changing atmospheric conditions and different integration times in each observing session means that the addition of the data has to be done in an especially careful way to get the most accurately calibrated final spectrum. Nevertheless, we would like to note that the presented data correspond to time averaged intensities as the lines in this source show a dependency of their intensity with stellar phase (Menten et al. 2012; Cernicharo et al. 2014; Pardo et al. 2018). We used reference strong lines to discard whole (or part of) observing sessions with technical or pointing problems. Then, we fitted the baselines to each FFTS section for each session after accumulating all valid scans in it. We avoid observations at very low elevations, less than ∼23 degrees, which would result in high noise. Then, we accumulated all sessions for each FFTS section, using the rms from the previous step as weighting factor. We fitted a new baseline to this result in smaller frequency ranges (200 MHz) than the FFTS sections themselves (2.5 GHz) to do a much finer job without degrading the original spectral resolution (38 kHz) at first. However, in the final product we applied a six-channel smoothing. This resulted in a final frequency resolution of $\Delta\nu$ = 229 kHz and a frequency dependent σ level, which is indicated in the upper panel of Fig. 1 and in each panel of Fig. 2.

3. Data analysis

For the final accumulated spectral results, we applied a global fit strategy, described in this section. First, we use as input the central line frequencies from the MADEX catalog (Cernicharo 2012), corresponding to molecular species that we already know to be present or expected in the data. To these we added all central frequencies associated to unidentified spectral features in the data. We developed a simple extended routine for multiline calculations using the same basic shape function from the SHELL method of the GILDAS[2] software package, expressed as

$$\phi(v) = \frac{A}{\Delta v} \frac{1 + 4H[(v - v_0)/\Delta v]^2}{1 + H/3}, \quad (1)$$

with A being the integrated intensity, v_0 the central frequency, Δv the full width at zero level (obtained from twice the terminal expansion velocity of the envelope, see below), and H the horn to center intensity ratio. The profile varies from a parabola ($H = -1$) for optically thick lines, a flat topped shape ($H = 0$), which corresponds to spatially unresolved optically thin lines, and a double-peaked profile ($H > 0$), which is produced by spatially resolved optically thin lines.

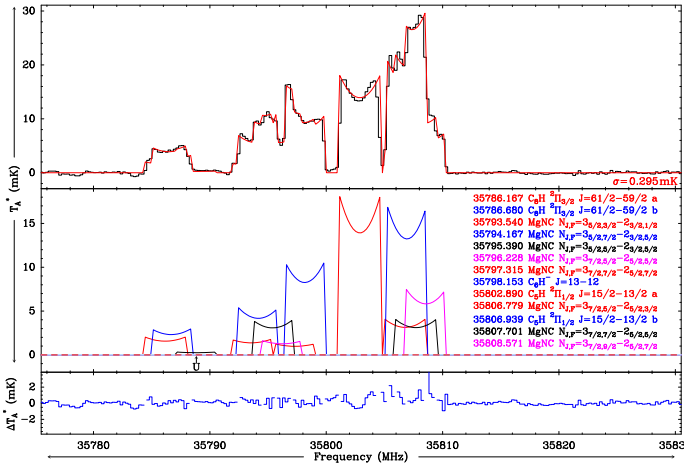

Fig. 1. Extreme example of global fit of IRC+10216 Q-band data to a series of individual lines (for $H = 0.3$) with integrated areas that can be obtained in a quite confident way, described in Section 3, despite the blending. The residuals from the global fit are plotted in the bottom panel. All spectral features present in the data, except a very small one, can be identified at present.

In our analysis, the LSR velocity of IRC+10216 has been fixed to −26.5 km s^{-1} and the terminal expansion velocity, v_{end}, of the envelope has been fixed to 14.5 km s^{-1} (Cernicharo et al. 2000). The H and A parameters depend for each line on the spatial distribution of the emission and on the line opacity. For most lines, we know that the emission appears in a shell with inner and external radii between 10 and 20″ and a thickness of 5–10″ (Agúndez et al. 2017). With very few exceptions, we found that $H = 0.3$ is a good value for our global fit calculations. This choice does not substantially affect the derived areas of the lines used for the rotation diagrams presented in this work.

The overall fit to the line profiles is built by creating a first guess table with values of v_0, A, and H for each expected (isolated or blended) spectral line. A synthetic spectrum is created from a line-by-line fit of A, with v_0 and H kept fixed, starting from the lowest frequency upwards. An iterative process is achieved to adjust the observed global line profile to the contribution of the individual lines. This iterative process runs nearly automatically, except for a few cases where the blending is so heavy that no realistic parameters can be obtained for some lines. In these cases, intervention into the analysis is necessary. After just a handful of steps, it is possible to have a first guess file from which the fitting of A for all lines produces variations of less than 10%. The adopted strategy provides excellent results: although it is common in our data to have several lines blended, in almost all cases it becomes possible to separate each one due to the similarity of the profiles and the use of information of other lines in each species' rotational ladder. Figure 1 gives an example of a very satisfactory line decomposition in IRC+10216 Q-band data. This has also been applied in previous IRC+10216 publications (see, e.g., Changala et al. 2022).

[2] http://www.iram.fr/IRAMFR/GILDAS

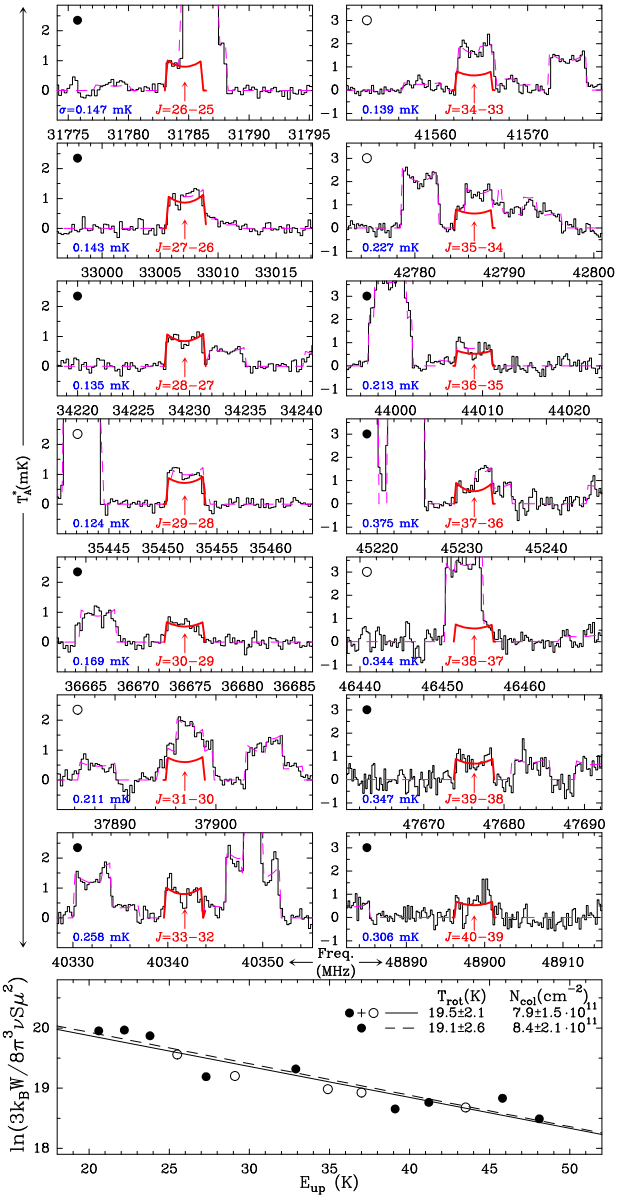

Fig. 2. SiC_6 lines observed in this work, with the fit for them in red. Black dots correspond to lines with no critical blending from other species while open dots identify lines heavily blended. The dashed magenta curves represent the overall fit for all lines according to the parameters given in Table 1. The bold red curves correspond to the contribution of the SiC_6 lines alone. The rms or σ values given for each spectrum in dark blue are calculated from the channels, with no signal in the fitted spectrum. The best-fit rotational diagrams using only the not heavily blended SiC_6 rotational transitions are shown separately as solid and dashed lines, respectively, in the bottom panel.

4. Results

Laboratory spectroscopy for SiC_6 is available from McCarthy et al. (2000). The molecule was implemented in MADEX adopting a dipole moment of 8.25 D as derived from ab initio calculations by the same authors. Although laboratory data only reach up to 20.8 GHz ($J = 17$), predictions for the rotational lines in the Q-band range ($J = 26$–25 up to $J = 40$–39) have uncertainties between 2 and 10 kHz. Hence, the estimated frequencies are well suited for searching this molecule in our data.

Table 1. SiC_6 lines and the spectral features near them, as modeled in Figure 2 with H from Equation (1) fixed to 0.3 and v_{end} = 14.5 kms^{-1}.

Molecule	μ (Debye)	Transition ID	ν_{ul} (MHz)	E_{up} (K)	Line Str.(S)	W (mK·km·s^{-1})
U31779			31778.709			4.573
SiC_6	**8.220**	**J = 26→25**	**31784.664**	**20.60**	**26.00**	**24.500**
$C_{10}H^-$	15.200	J = 53→52	31785.863	41.20	53.00	63.157
C_4H v_7=1	2.100	see [1]	31786.650	247.10	2.39	41.758
SiC_6	**8.220**	**J = 27→26**	**33007.120**	**22.20**	**27.00**	**27.754**
U33008			33008.406			5.471
U33010			33010.335			3.649
SiC_6	**8.220**	**J = 28→27**	**34229.572**	**23.80**	**28.00**	**28.047**
$H^{13}CCC^{15}N$	3.732	J = 4→3	34233.231	4.10	4.00	8.319
CH_3C_5N	5.400	$J = 22_0 \rightarrow 21_0$	34233.376	18.90	22.00	7.577
U35441			35440.971			9.568
HC_9N	5.200	J = 61→60	35442.454	52.70	61.00	143.684
SiC_6	**8.220**	**J = 29→28**	**35452.020**	**25.50**	**29.00**	**22.721**
U35453			35452.518			8.466
l-HC_4N	4.330	$N_J = 8_7 \rightarrow 7_6$	36666.112	8.40	6.91	26.789
SiC_6	**8.220**	**J = 30→29**	**36674.464**	**27.30**	**30.00**	**17.271**
HC_9N v_{19}=3	5.200	$J_L = 65_{-1} \rightarrow 64_{-1}$	37888.364	276.60	65.00	14.666
$C^{13}CCCH$	2.100	see [2]	37896.002	4.50	2.29	9.480
SiC_6	**8.220**	**J = 31→30**	**37896.904**	**29.10**	**31.00**	**19.114**
$HC^{13}CC_5N$	4.820	J = 34→33	37897.938	31.80	34.00	28.044
CH_2CHCNa	3.821	$J_{K,k} = 4_{0,4} \rightarrow 3_{0,3}$	37904.851	4.50	4.00	29.085
U37907			37906.800			11.841
U40332			40332.097			37.223
U40335			40335.000			10.764
SiC_6	**8.220**	**J = 33→32**	**40341.773**	**32.90**	**33.00**	**25.301**
MgC_5N	7.300	$N_J = 35\frac{69}{2} \rightarrow 34\frac{67}{2}$	40348.015	34.90	34.50	53.699
MgC_5N	7.300	$N_J = 35\frac{71}{2} \rightarrow 34\frac{69}{2}$	40349.822	34.90	35.50	43.479
U41559			41558.500			8.209
SiC_6	**8.220**	**J = 34→33**	**41564.200**	**34.90**	**34.00**	**20.054**
$HCC^{13}CC_4N$	4.820	J = 37→36	41564.473	37.90	37.00	30.450
U41567			41567.000			7.111
$HC_4C^{13}CCN$	4.820	J = 37→36	41574.391	37.90	37.00	41.439
HC_5N v_{11}=2	4.330	J = 16→15	42780.600	325.70	48.00	63.374
SiC_6	**8.220**	**J = 35→34**	**42786.623**	**37.00**	**35.00**	**19.810**
U42788			42787.655			26.468
$H^{13}CCC^{15}N$	3.732	J = 5→4	42791.453	6.20	5.00	20.019
U42794			42794.200			18.733
$C_8H^2\Pi_{3/2}$	6.500	$J = \frac{75}{2} \rightarrow \frac{73}{2}$ a 1	43999.034	40.50	74.90	58.626
$C_8H^2\Pi_{3/2}$	6.500	$J = \frac{75}{2} \rightarrow \frac{73}{2}$ b	43999.793	40.50	74.90	57.243
$HCC^{13}C^{15}N$	3.732	J = 5→4	44007.159	6.30	5.00	6.288
SiC_6	**8.220**	**J = 36→35**	**44009.042**	**39.10**	**36.00**	**16.118**
$HCC^{13}CCCN$	4.330	J = 17→16	45217.843	19.50	17.00	252.488
$HCCC^{13}CCN$	4.330	J = 17→16	45223.345	19.50	17.00	244.703
SiC_6	**8.220**	**J=37→36**	**45231.455**	**41.20**	**37.00**	**19.149**
$H^{13}CC_6N$	4.820	J = 41→40	45233.690	45.60	41.00	21.366
$C_7H^2\Pi_{3/2}$	5.945	$J,= \frac{53}{2} \rightarrow \frac{51}{2}$	46452.599	68.20	106.00	86.785
SiC_6	**8.220**	**J = 38→37**	**46453.864**	**43.50**	**38.00**	**18.668**
HC_7N v_{15}=3	4.820	$J_L = 40_{-3} \rightarrow 39_{-3}$	46466.395	315.50	40.80	3.494
HC_7N v_{15}=3	4.820	$J_L = 40_3 \rightarrow 39_3$	46466.591	315.50	40.80	3.494
SiC_6	**8.220**	**J = 39→38**	**47676.268**	**45.80**	**39.00**	**23.017**
S3		$J = \frac{81}{2} \rightarrow \frac{79}{2}$	47683.300			24.534
U47691			47691.450			23.674
S4		$J = \frac{83}{2} \rightarrow \frac{81}{2}$	48883.000			14.165
SiC_6	**8.220**	**J = 40→39**	**48898.666**	**48.10**	**40.00**	**17.244**

Notes. The area of the line W in mK·kms^{-1} is derived from the only free parameter for each line in the fit which is the integrated intensity A in Equation (1). S3 and S4 are the unknown carriers of two series of lines identified in the data to which even the quantum numbers can be assigned. Other unidentified lines are labeled as UXXXXX with the rounded value in MHz from their central frequencies. [1] (N,P,J,F) = (3,1,7/2,3)→(2,–1,5/2,2) [2] $(N,J)_{f,F} = (4,7/2)_{3,5/2} \rightarrow (3,5/2)_{2,3/2}$.

Figure 2 shows the accumulated results of our Yebes-40m IRC+10216 Q-band integration as of September 15, 2024, around the expected positions of SiC_6 rotational transitions, with the global fit superimposed. From this figure, we get the line parameters listed in Table 1 that have been used for deriving the rotational temperature and column density of SiC_6 from a rotation diagram linear regression (also plotted on Figure 2). One of the lines (J = 32→31) has been eliminated from the analysis because it is strongly affected by RFI signals around 39.0–39.25

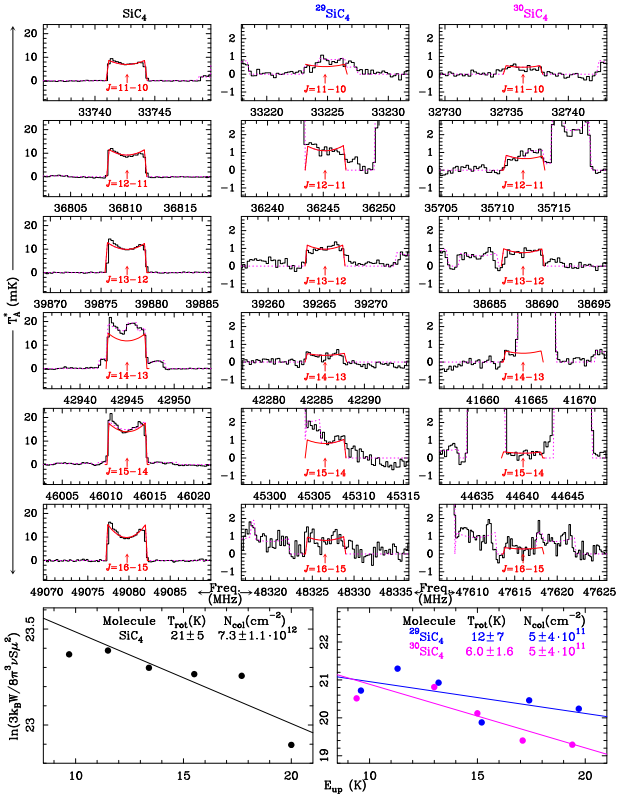

Fig. 3. SiC_4, $^{29}SiC_4$, and $^{30}SiC_4$ lines found in this work, with their fitted line profile shown in red. The dotted magenta curves represent the overall fit that takes into account all lines in the data.

GHz. The J = 30→29 line, kept in the figure and in the analysis, may also suffer from the same problem but to a much lower extent. Otherwise, the rotation diagram appears to be very consistent and the results of the linear regression do not show any significant changes when the most heavily blended SiC_6 lines are included and when they are not.

A similar analysis was performed on SiC_4, with the results shown on Figure 3. From the intensities found for the J = 11→10 to J = 16→15 transitions of this molecule and the $^{28}Si/^{29}Si$ and $^{28}Si/^{30}Si$ isotopic ratios in this source (15.4 and 20.3, respectively; Cernicharo et al. 2000), along with the current sensitivity of the survey, we expect to detect $^{29}SiC_4$ (comfortably) as well as $^{30}SiC_4$ (more marginally). Both species are also included Figure 3. The four ^{13}C substitutions were searched for, but they do not appear in the data above the current noise level, which was anticipated. Some of the lines in Figure 3 are blended with other species but, due to space limitation, we omit these details.

We could think about adding SiC_2 to this analysis. However, this species is a ring with a C_{2v} symmetry, it is light and has only three detected transitions in our *Q*-band survey with line strengths spanning three orders of magnitude, making the simple rotation diagram analysis difficult and uncertain with only those lines. We can say, however, that the column densities of SiC_4 and SiC_6 are more than two orders of magnitude below those derived for SiC_2 and Si_2C by Cernicharo et al. (2015, 2018) and Massalkhi et al. (2018) using an extended range of frequencies.

5. Discussion and conclusions

The chemistry of SiC_6 in IRC +10216 has not been studied to our knowledge, but that of SiC_4 has been discussed to some extent. Ohishi et al. (1989) proposed that SiC_4 could be formed in neutral-neutral reactions of SiC_2 with C_2H_2 and C_2H or through ion schemes starting with the reaction of Si^+ and C_2H_2. In the chemical model of MacKay & Charnley (1999), SiC_4 is mainly formed in the external circumstellar layers through the reaction between SiC_2 and C_2H. Schemes based on neutral-neutral reactions or ion-neutral reactions could be behind the synthesis of SiC_4 and SiC_6 in IRC +10216. Within the first category, reactions of the type

$$Si + C_nH \rightarrow SiC_n + H, \qquad SiC_2 + C_nH \rightarrow SiC_{n+2} + H \qquad (2)$$

arise as very promising routes to the synthesis of SiC_4, SiC_6, and even longer Si-bearing carbon chains, although detailed theoretical calculations are needed to shed light on whether these reactions are barrierless and proceed through H atom elimination. In the second category, experimental data support the reactivity of the cation Si^+ with unsaturated carbon chains. However, the products formed, namely, SiC_2H^+ + H in the case of acetylene and C_4H^+ + SiH in the case of diacetylene (Wlodek et al. 1991), indicate that the synthesis is probably not straightforward and may involve several steps of carbon chain growth. This could include reactions between cations SiC_nH^+ and unsaturated hydrocarbons such as C_2H_2 and C_2H. A mechanism similar to that proposed by Petrie (1996) for the formation of metal-bearing carbon chains would be based on the radiative association of Si^+ with a neutral carbon chain, followed by the dissociative recombination of the ionic complex formed. This approach could also contribute to the formation of silicon-bearing carbon chains in IRC +10216, similarly to the scenario reported here.

Acknowledgements. This work uses data obtained through projects 19A010, 20A017, 20B014 and 21A019 of the Yebes Observatory 40 m radio telescope, operated by the Spanish Instituto Geográfico Nacional (IGN, Ministerio de Transportes y Movilidad Sostenible). We thank the ERC for funding through grant ERC-2013-Syg-610256-NANOCOSMOS, and the Spanish Ministerio de Ciencia, Innovación y Universidades (MICIU), FEDER and ESF+ for funding support through grants PID2023-147545NB-I00, PID2022-137980NB-I00 and RYC2023-045648-I.

References

Agúndez, M., Cernicharo, J., Quintana-Lacaci, G., et al. 2017, A&A, 601, A4
Cabezas, C., Pardo, J. R., Agúndez, M., et al. 2023, A&A, 672, L12
Cernicharo, J. 1985, Internal IRAM report (Granada: IRAM)
Cernicharo, J. 2012, EAS Publ. Ser., 2012, 251
Cernicharo, J., Guélin, M., & Kahane, C. 2000, A&AS, 142, 181
Cernicharo, J., Teyssier, D., Quintana-Lacaci, G., et al. 2014, ApJ, 796, L21
Cernicharo, J., McCarthy, M. C., Gottlieb, C. A., et al. 2015, ApJ, 806, L3
Cernicharo, J., Guélin, M., Agúndez, M., et al. 2018, A&A, 618, A4
Cernicharo, J., Cabezas, C., Pardo, J. R., et al. 2019, A&A, 630, L2
Cernicharo, J., Cabezas, C., Pardo, J. R., et al. 2023a, A&A, 672, L13
Cernicharo, J., Pardo, J. R., Cabezas, C., et al. 2023b, A&A, 670, L19
Changala, P. B., Gupta, H., Cernicharo, J., et al. 2022, ApJ, 940, L42
Gupta, H., Changala, P. B., Cernicharo, J., et al. 2024, ApJ, 966, L28
MacKay, D. D. S., & Charnley, S. B. 1999, MNRAS, 302, 793
Massalkhi, S., Agúndez, M., Cernicharo, J., et al. 2018, A&A, 611, A29
McCarthy, M. C., Apponi, A. J., Gottlieb, C. A., et al. 2000, ApJ, 538, 766
Menten, K. M., Reid, M. J., Kamińsky, T., & Claussen, M. J. 2012, A&A, 543, A73
Ohishi, M., Kaifu, N., Kawaguchi, K., et al. 1989, ApJ, 345, L83
Pardo, J. R., Cernicharo, J., & Serabyn, E. 2001, IEEE Trans. Ant. Propag., 49, 12
Pardo, J. R., Cernicharo, J., Velilla-Prieto, L., et al. 2018, A&A, 615, L4
Pardo, J. R., Cabezas, C., Fonfría, J. P., et al. 2021, A&A, 652, L13
Pardo, J. R., Cernicharo, J., Tercero, B., et al. 2022, A&A, 658, A39
Pardo, J. R., De Breuck, C., Muders, D., et al. 2025, A&A, 693, A148
Petrie, S. 1996, MNRAS, 282, 807
Tercero, F., López-Pérez, J. A., Gallego, J. D., et al. 2021, A&A, 645, A37
Wlodek, S., Fox, A., & Bohme, D. K. 1991, J. Am. Chem. Soc., 113, 4461